Journal of Magnetic Resonance 193 (2008) 191–198

Contents lists available at ScienceDirect

Journal of Magnetic Resonance

journal homepage: www.elsevier.com/locate/jmr

Development and testing of a CW-EPR apparatus for imaging of short-lifetime nitroxyl radicals in mouse head

Hideo Sato-Akaba [a], Hirotada Fujii [b], Hiroshi Hirata [a,c,*]

[a] Department of Electrical Engineering, Yamagata University, Yonezawa, Yamagata 992-8510, Japan
[b] School of Health Sciences, Sapporo Medical University, Sapporo 060-8556, Japan
[c] Graduate Program of Human Sensing and Functional Sensor Engineering, Yamagata University, Yonezawa, Yamagata 992-8510, Japan

ARTICLE INFO

Article history:
Received 14 February 2008
Revised 20 April 2008
Available online 29 April 2008

Keywords:
3D EPR imaging
Uniform distribution of projections
Nitroxyl radicals
Geodesic sphere

ABSTRACT

This article describes a method for reducing the acquisition time in three-dimensional (3D) continuous-wave electron paramagnetic resonance (CW-EPR) imaging. To visualize nitroxyl spin probes, which have a short lifetime in living organisms, the acquisition time for a data set of spectral projections should be shorter than the lifetime of the spin probes. To decrease the total time required for data acquisition, the duration of magnetic field scanning was reduced to 0.5 s. Moreover, the number of projections was decreased by using the concept of a uniform distribution. To demonstrate this faster data acquisition, two kinds of nitroxyl radicals with different decay rates were measured in mice. 3D EPR imaging of 4-hydroxy-2,2,6,6-tetramethylpiperidine-d_{17}-1-^{15}N-1-oxyl in mouse head was successfully carried out. 3D EPR imaging of nitroxyl spin probes with a half-life of a few minutes was achieved for the first time in live animals.

1. Introduction

It is challenging to detect free radicals that have a short lifetime in living organisms. To visualize free radical molecules in mice or rats with electron paramagnetic resonance (EPR) imaging, data acquisition should be faster than the decay of the free radical molecules being measured. In the first biological EPR imaging study [1], 3-carboxamido-2,2,5,5-tetramethylpyrroline-1-oxyl (CTPO) was used as a free radical spin probe. After this work, 5-membered nitroxyl radicals were widely used in most EPR imaging studies [2–5]. The major reason for the use of five-membered spin probes, such as CTPO, was that they had longer lifetimes in subject animals. Otherwise, a data set of spectral projections for reconstructing an EPR image could not be obtained before the spin probes disappeared. If the acquisition time of EPR imaging is shorter than the lifetime of six-membered spin probes, there should be no reason to exclude the use of six-membered nitroxyl radicals, such as 4-hydroxy-2,2,6,6-tetramethyl-piperidinooxy (TEMPOL), which has a half-life of a few minutes in live animals.

Faster data acquisition would allow us to use any kind of useful nitroxyl probe, either five- or six-membered, for in vivo EPR imaging studies. Three-dimensional (3D) continuous-wave (CW) EPR imaging is suitable for visualizing a variety of free radical molecules in living animals. However, data acquisition for 3D EPR images takes a relatively longer time in comparison to a short lifetime of six-membered nitroxyl spin probes in live animals. To date, seminal works have been reported on the challenge of reducing the acquisition time in CW-EPR imaging. Demsar et al. reported EPR imaging at 9.5 GHz for phantoms with an acquisition rate of 6 s/projection in 1988 [6]. Ishida et al. reported EPR spectroscopy with an acquisition rate of 48 s/spectrum in the rat head in 1989 [7]. Alecci et al. reported in vivo EPR imaging of rat tails at 1.2 GHz with an acquisition rate of 3.5 s/projection in 1990 [8]. Moreover, Ishida et al. reported EPR imaging in the rat head with an acquisition rate of 30 s/projection in 1992 [9]. Yokoyama et al. reported their 700-MHz EPR imager with an air-core Helmholtz coil pair that achieved an acquisition rate of 1.4 s/projection in 1996 [10]. Recently, Samouilov et al. reported in vivo 3D EPR imaging at 1.2 GHz for live mice with an acquisition rate of 1.3 s/projection in the context of EPR/NMR co-registration imaging [11]. In addition to a fast-scan approach, the concept of the uniform distribution of projections is useful for further reducing the acquisition time of a data set of 3D projections [12–15]. Although there has been significant progress in EPR instrumentation as described above, 3D EPR imaging of short-lifetime nitroxyl radicals, such as TEMPOL, in living animals has not yet been demonstrated. 3D EPR imaging of TEMPOL in isolated rat hearts was reported by Kuppusamy et al. [16]. However, the lifetime of TEMPOL was prolonged in the presence of polynitroxyl-albumin (PNA).

The goal of the present work was to demonstrate in vivo 3D CW-EPR imaging with six-membered nitroxyl spin probes that

* Corresponding author. Address: Department of Electrical Engineering, Yamagata University, Yonezawa, Yamagata 992-8510, Japan. Fax: +81 238 26 3299.
E-mail address: hhirata@yz.yamagata-u.ac.jp (H. Hirata).

1090-7807/$ - see front matter © 2008 Elsevier Inc. All rights reserved.
doi:10.1016/j.jmr.2008.04.035

have a half-life of a few minutes in animals. We reduced the scanning time of a single spectrum, and used a uniform distribution of projection. In 3D image reconstruction, we used one-step filtered back projection (FBP). An acquisition time of 30 s for in vivo EPR imaging was achieved under the condition of 46 projections and a single scan of 0.5 s per projection. This enabled us to obtain in vivo 3D images of mouse heads with 4-hydroxy-2,2,6,6-tetramethylpiperidine-d_{17}-1-^{15}N-1-oxyl (TEMPOL-d_{17}, $-^{15}$N) probes.

2. Methods

2.1. EPR imager

A home-built 650-MHz EPR spectrometer, with three sets of gradient coils that generated magnetic field gradients along the *X*-, *Y*-, and *Z*-directions, was used. Fig. 1 shows a diagram of the EPR imager used in the present study. EPR signals were obtained in conjunction with a digital lock-in amplifier (LI 5640, NF Corp., Yokohama, Japan) and magnetic field modulation at 90 kHz. An analog output (EPR signals) of the lock-in amplifier was delivered to a multifunction data acquisition board (6034E, National Instruments, Austin, TX). Data acquisition was started by a trigger pulse coming from a bipolar power supply (PBX20-10, Kikusui Electronics Corp., Yokohama, Japan) that was used for magnetic field scanning. This trigger makes good synchronization of data acquisition possible for each projection. For magnetic field gradients in the *X*-, *Y*-, and *Z*-directions, the gradient coils were individually driven by bipolar power supplies (PBX20-10). A Maxwell coil pair (100 mm in diameter) was used to generate the field gradient in the *Z*-direction, and two sets of pair coils were used to generate field gradients in the *X*- and *Y*-directions. The currents of the bipolar power supplies were set by a personal computer (PowerMac G5, Apple, Cupertino, CA) via an IEEE-488 interface bus. Data acquisition and setting of measurement parameters were controlled by a program that was written in the LabVIEW™ 8.2 development environment on MacOS X.

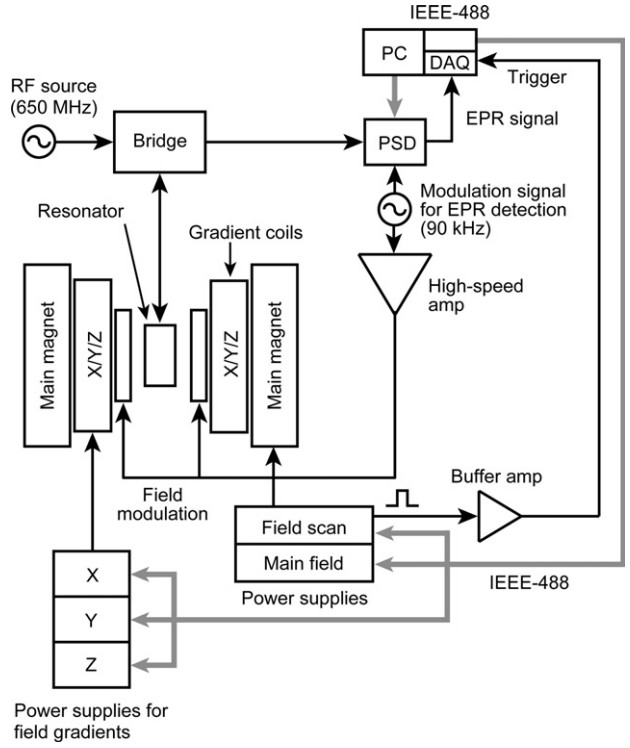

Fig. 1. Schematic diagram of a 650-MHz CW-EPR imager. A bipolar power supply for field scanning triggered data acquisition of EPR signals. A lock-in amplifier was used for phase-sensitive detection (PSD) for EPR signal detection, and the detected signals were delivered to a multifunction data acquisition board (DAQ). Bipolar power supplies and a DC power supply were controlled with a personal computer (PC) via an IEEE-488 interface bus. Trigger pulses generated by the power supply for field scanning were transmitted to a trigger port of the DAQ.

A water-cooled resistive Helmholtz coil pair (400 mm in average diameter) was used to generate a static magnetic field in the *Z*-direction. Magnetic field scanning was carried out with another Helmholtz coil pair (130 mm in diameter), which was placed inside the main-field Helmholtz coil, and a bipolar power supply. This Helmholtz coil pair and the power supply (±10 A) achieved field scanning of 13 mT. Such a scanning width is sufficient to cover hyperfine splitting for EPR spectra of the nitroxyl radicals we used. The inductance and resistance of the Helmholtz coil pair for field scanning were 0.68 mH and 1.2 Ω, respectively. The time constant of the Helmholtz coil pair was 0.57 ms, which is small enough for the ramp sweep time of 0.5 s. A saddle-type coil (44 mm in diameter and 80 mm in length) was used for magnetic field modulation. This saddle-type coil was designed to achieve magnetic field modulation of greater than 0.3 mT (peak-to-peak), which is larger than the intrinsic line-widths for EPR spectra of nitroxyl radicals. A high-speed amplifier (4015, NF Corp., Yokohama, Japan) drove the modulation coil. We used a function generator (33210 A, Agilent Technologies, Palo Alto, CA) for the modulation signals of field modulation at 90 kHz.

A multi-coil parallel-gap resonator (MCPGR) with an inner diameter of 24 mm and length of 34 mm was used to measure the phantom and the head of a mouse [17]. These dimensions of the resonator were chosen to cover the head of a mouse. A matching circuit that used a capacitor in a parallel connection was used to excite the resonator [18]. The unloaded quality factor was 490, and this decreased to 170 when the head of a mouse was inserted. The resonator does not have an electric shielding plate inside the loops. The absence of a shielding plate near the gap (the parallel plate capacitor) decreases the quality factor because of Joule heating in biological samples. Eddy currents due to RF magnetic fields in biological samples also decrease the quality factor. This eddy-current-related loss cannot be avoided even if a shielding plate exists near the gap. The RF magnetic field and electric field were not completely separated in the resonator. However, its impact on the quality factor or loss of the resonator was not crucial in our experiments. The efficiency of the resonator for generating an RF magnetic field was 44 $\mu T/W^{1/2}$ at the center of the resonator, when it was empty. This was measured by the metal perturbing sphere method [19,20]. The axis of the resonator was parallel to the *Y*-direction. For measurement in a living mouse, automatic tuning control (ATC) for the RF resonator was introduced by varactor diodes.

The microwave bridge could apply a maximum microwave power of 50 mW to the resonator. With this power level, the EPR signal from nitroxyl spin probes could be slightly saturated. In the experiments, the microwave power applied to the resonator was optimized to increase the signal-to-noise ratio (SNR). The spectra of our samples were obtained in the linear region and not saturated (data not shown). A reflection-type bridge was formed with a 180-degree hybrid (H-1-4, M/A-Com, Lowell, MA). The RF signals were delivered from an RF synthesizer (MG3633A, Anritsu Corp., Kanagawa, Japan), and boosted with a low-noise amplifier (ZRL-700, Mini-Circuits Laboratory, Brooklyn, NY). We used this amplifier to apply a microwave power of 50 mW to the resonator. This microwave power was needed to increase the signal intensity of EPR spectra when an animal subject is placed in the resonator. The signals received from the resonator were amplified with a low-noise amplifier (AFS1-00500100-08-10P-4, Miteq, Hauppauge, NY). This low-noise amplifier has a noise figure of

0.7 dB, and we choose a low-noise amplifier to keep the noise figure as low as possible. For RF detection, we used an RF Schottky barrier diode (Agilent Technologies, HSMS-2820).

2.2. Uniform distribution of projections

To decrease the acquisition time, a uniformly distributed set of projection data which avoids a large overlap of projections at the poles, rather than a conventional distribution over equal polar and azimuthal grids, is favorable, although the time required to calculate 3D image-reconstruction with the one-step FBP method is longer than that with the two-step FBP method [12]. Depending on the reconstruction algorithm, the choice of the projection can be classified into two categories; a non-uniform distribution, which is suitable for two-step reconstruction, and an approximately uniform distribution, which is suitable for one-step reconstruction. Most previous studies on 3D EPR imaging have used two-step FBP to decrease the calculation time. However, the one-step FBP method is no longer as time-consuming because of recent advances in computers.

To improve the uniform distribution without complicated calculations such as a quasi-Monte Carlo method [13], the vertices of the geodesic spheres generated from an icosahedron were used in this study. The vertices of the icosahedron and its geodesic sphere were obtained using a function in the standard package of Mathematica 5 (Wolfram Research, Inc., Champaign, IL). The original 20 faces in an icosahedron are congruent and therefore the vertices are uniformly distributed in the circumscribed sphere. To increase the number of vertices, which would mean an increase in the number of projections, each face of an icosahedron was tessellated regularly onto the circumscribed sphere. Therefore, the number of projections depends on the order of m regular tessellations for each face of the icosahedron. Fig. 2 shows the polyhedrons produced from 162 vertices generated from a geodesic sphere of an icosahedron with $m = 4$ and from an equal interval of $\Delta\phi = \Delta\theta = \pi/9$, where ϕ is the polar angle and θ is the azimuth angle.

2.3. Data acquisition and image-reconstruction

To decrease the effect of signal decay on a reconstructed image, signal averaging was not performed during data acquisition for 3D EPR imaging. The sequence of current flow into the Helmholtz coil pair that was used for magnetic field scanning was programmed in a bipolar power supply before data acquisition of EPR spectra was started. Fig. 3 shows the timing chart for field scanning, magnetic field gradients, and data acquisition. A trigger pulse was generated by the power supply when a ramp-signal started, and was used to synchronize data acquisition. First, the zero field-gradient EPR spectrum was measured for deconvolution of the spectra obtained under field gradients. After the spectrum was measured, the amplitudes of currents flowing into the field gradient coils were set for acquisition of the next projection data. Data acquisition was continued to measure the next set of projections for 3D imaging until the EPR signal from the spin probes in the subject mouse became weak. In a single EPR spectrum, 512 points were acquired.

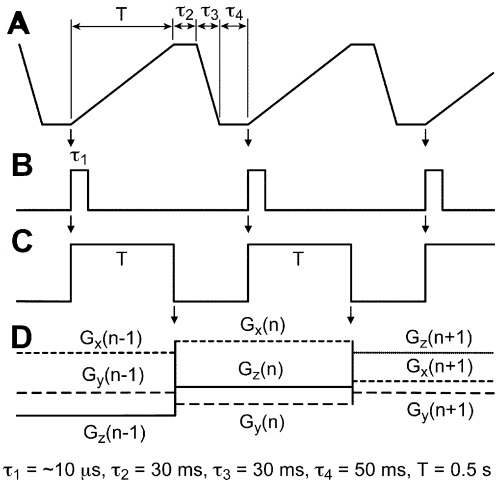

Fig. 3. Timing chart for data acquisition. (A) Field scanning driven by a bipolar power supply, (B) trigger pulse generated by the power supply, (C) status of the data acquisition board, and (D) field gradients in the *X*-, *Y*-, and *Z*-directions. After data acquisition for the *n*th projection, the field gradients are set for the next projection.

3D image-reconstruction was carried out by the FBP method, and the reconstruction code was written in FORTRAN (Pro Fortran 10, Absoft Corp., Rochester Hills, MI). Image-reconstruction based on one-step FBP with a uniform distribution of projections has been reported elsewhere [12–15]. In image-reconstruction, we used a Hamming filter to suppress noise in a process of deconvolution. Surface-rendered images and 2D slice images were drawn using IDL 6.4 data visualization software (ITT Visual Information Solutions, Boulder, CO).

2.4. Chemicals

4-Hydroxy-2,2,6,6-tetramethylpiperidine-d_{17}-1-^{15}N-1-oxyl (TEMPOL-d_{17}, $-^{15}$N) was purchased from CDN Isotopes Inc. (Quebec, Canada). 3-Hydroxymethyl-2,2,5,5-tetramethylpyrrolidine-1-oxyl (hydroxymethyl-PROXYL) was obtained from Toronto Research Chemicals Inc. (Ontario, Canada). All nitroxyl compounds examined in animal study were dissolved in phosphate-buffer saline (PBS, pH 7.4).

2.5. Phantom imaging

To validate our approach which uses the uniform distribution of projections and sub-second field scanning in EPR imaging, three capillary tubes (1.9 mm inner diameter (i.d.), 2.4 mm outer diameter (o.d.), 20 mm in length) containing 1 mM TEMPOL-d_{17}, $-^{15}$N in distilled water were measured as a phantom. To investigate the effects of the distribution and number of projections on the quality of the images, low-noise EPR spectra were needed for image-reconstruction. Thus, we did not use saline solution, which gives a loss of electromagnetic waves in the resonator, for a phantom. The lowest field absorption peak of TEMPOL-d_{17}, $-^{15}$N was measured with a 2-mT field sweep. To compare the quality of the images, the total scan time (duration of a single field scan $\times$ number of projections $\times$ number of averagings) was kept approximately constant (7 min) for 46 and 81 uniform projections, and for 49, 81, and

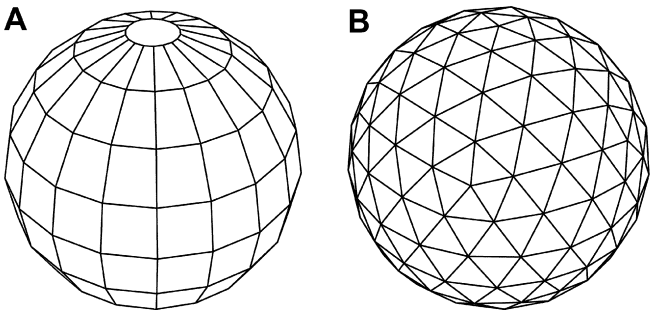

Fig. 2. Distribution of the vertices of the polyhedron, the angles of which are directions of the projections. (A) Non-uniform distribution. (B) Approximately uniform distribution. In both polyhedrons, there are 81 vertices in a hemisphere.

144 non-uniform conventional projections. To evaluate the effects of the number of projections, choice of projections, and single scan time on image quality, a Hamming filter with the same cut-off frequency was used to decrease noise in the high-frequency band.

The parameters of EPR imaging for the phantom were as follows: RF power 20 mW, field scanning 2 mT, magnetic field modulation 0.1 mT, field gradient 60 mT/m, single scan time 0.5 or 0.15 s, time constant of the lock-in amplifier 1.0 or 0.3 ms, and number of projections 46, 49, 81, 144, or 181. The correlation coefficients that were used to examine the image quality were calculated with an image produced from 181 uniformly distributed projections. The correlation coefficients were calculated for volumes in which the image intensity was more than half of the maximum intensity.

2.6. Animal experiments

Male ICR mice were obtained from Charles River Japan, Yokohama, Japan. The mice were 6 weeks of age and weighed 30 g. They were maintained on laboratory chow and water *ad libitum* on a 12-h light/dark cycle. Mice were anesthetized by the intraperitoneal (i.p.) injection of Nembutal (45 mg/kg body weight). After anesthetized mice were set on the resonator of the EPR imaging system, they received 0.2-0.25 ml of 200 mM TEMPOL-d_{17}, $-^{15}N$ or hydroxymethyl-PROXYL via intraperitoneal injection. The protocols for all animal experiments were approved by the Yamagata University School of Engineering Animal Care Committee and by the Sapporo Medical University Animal Care Committee according to the National Institutes of Health Animal Care and Use Protocol (USA).

2.7. Imaging of live mice

Data acquisition was started just after one of the spin probes was infused into a subject mouse. The signal that appeared at a lower field was measured with a 2-mT field sweep. The total acquisition time for a single 3D image was 30 s and 51 s for 46 and 81 projections, respectively. While the estimated acquisition time was 23.5 s for 46 projections and one zero gradient-spectrum (0.5 s × 47 scans), a waiting period is needed to stabilize the magnetic field and field gradients for each projection. Thus, 30 s was needed to acquire 47 spectra. Data acquisition was continuously performed until the signal intensity became weak. To compensate for the decay of EPR signals during data acquisition of 46 or 81 projections, the signal intensities of each projection were normalized based on linear interpolation between two successive zero gradient-spectra. The measurement parameters in EPR imaging with mice were as follows: RF power 32 mW, field scanning 2 mT, magnetic field modulation 0.1 mT, field gradient 40 mT/m, duration of field scanning 0.5 s, and time constant of the lock-in amplifier 1 ms.

In proton-MRI experiments, the multislice spin echo sequence was used with the following parameters: TR 500 ms, TE 8 ms, field-of-view (FOV) 38 × 38 mm, image matrix 256 × 256, NEX 8, and slice thickness 4 mm.

3. Results

3.1. Delay and correction of EPR spectra

To verify that our spectrometer could rapidly acquire EPR signals, we measured the EPR spectra of 1 mM TEMPOL-d_{17}, $-^{15}N$ in distilled water (0.5 ml) with various scan times. The total acquisition time (duration of single field scanning × number of averagings) was kept constant at 60 s. The doublet signal due to the hyperfine splitting of ^{15}N was observed. As shown in Fig. 4, the position of the signal shifted when field scanning became fast. The signal shift was due to the rise/fall time attributed to the bipolar power supply. The time constant (0.57 ms) of the coil used for field scanning did not affect the rise/fall time of field scanning, where the time constant is negligibly small in comparison to the scan time. Since we did not use a Hall probe to measure the magnetic field during the measurements, the magnitude of the center field in the spectra was calculated from the microwave carrier frequency and *g*-factor of spin probes in a slowly scanned EPR spectrum. Thus, the delay of field scanning caused the shift in the measured spectra. To compensate for the delay in field scanning, data acquisition can be delayed using a delayed trigger pulse from the power supply. The actual scan-width of the magnetic field decreased as the scan time became shorter. However, the lineshape of the measured spectra can be scaled by $B_{\text{corrected}} = \alpha(B + B_{\text{shift}})$, as shown in Fig. 4. The coefficients α and B_{shift} are summarized in Table 1.

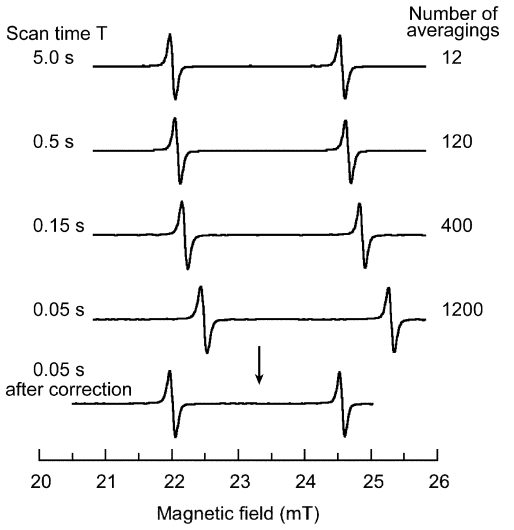

Fig. 4. EPR spectra of 1 mM TEMPOL-d_{17}, $-^{15}N$ in distilled water (0.5 ml) obtained under a scan time of 5.0, 0.5, 0.15, and 0.05 s. The bottom trace was obtained after the magnetic field of the spectrum (scan time of 0.05 s) was scaled by the coefficients in Table 1. The measured SNRs of EPR spectra are given in Table 1.

The effects of the duration of field scanning on the SNRs for the measured spectra are summarized in Table 1. To reduce the duration of field scanning, the time constant (integration time) of a lock-in amplifier must be reduced to avoid the distortion of EPR spectra. This leads to lower SNRs for single-scan EPR spectra. Therefore, in practice, the achievable duration of field scanning depends on the sensitivity of the EPR spectrometer and the given measurement duration.

3.2. Phantom imaging

Fig. 5 shows a photograph of the phantom and surface-rendered 3D images of TEMPOL-d_{17}, $-^{15}N$ in three capillary tubes measured

Table 1
Effects of the duration of field scanning on the signal-to-noise ratio of EPR spectra and scaling coefficients for a magnetic field

Scan time (s)	Time constant (ms)	SNR (single scan)	SNR (number of averagings)	α	B_{shift} (mT)
5.00	10	182.5 ± 37.6	680 (12)	1.00	0.0
0.50	1	62.1 ± 13.4	780 (120)	0.99	−0.044
0.15	0.3	34.9 ± 8.8	680 (400)	0.96	−0.850
0.05	0.1	20.1 ± 5.1	640 (1200)	0.90	−1.840

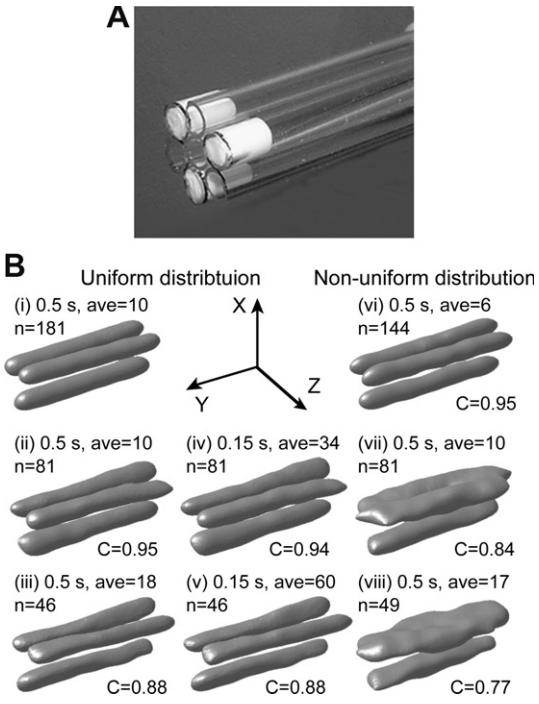

Fig. 5. Phantom imaging of TEMPOL-d_{17}, $-^{15}N$ in capillary tubes (1.9 mm i.d.). (A) Photograph of the capillary tubes. Three tubes were filled with 1 mM TEMPOL-d_{17}, $-^{15}N$ solution. (B) 3D EPR images of the capillary tubes. The scan time (0.5 or 0.15 s), number of averagings (ave), number of projections (*n*), and correlation coefficient (C) are also shown. The correlation coefficient of the image being tested was calculated with the image (i) in the upper left corner as a reference.

with different projections and different field scanning times. The intensities of the images were normalized by the maximum intensity in each image. The images generated from 49 and 81 projections of non-uniform distributions showed scattered or unresolved results. A visual inspection and the correlation coefficient indicated that the quality of the image (Fig. 5B (iii)) generated from 46 projections with a uniform distribution exceeded that for the image (Fig. 5B (vii)) generated from 81 projections with a non-uniform distribution. As shown in Fig. 5, the quality of the image measured with 0.5-s field scanning was similar to that with 0.15-s field scanning. The level of the isosurface was set at half of the maximum intensity in each image. The reconstruction time for a 3D image ($128 \times 128 \times 128$ voxels) was 5 s on a Mac Pro personal computer (two dual-core Intel Xeon 2.66 GHz, Apple Cupertino, CA), using 81 projections and the one-step FBP method.

3.3. In vivo imaging in mice

To prove that our data acquisition is faster than the decay of nitroxyl spin probes, we show the temporal change in EPR signal intensity in Fig. 6. A data acquisition time of 30 s for a single 3D image is reasonably fast for the decay of TEMPOL-d_{17}, $-^{15}N$ in an examined animal. The signal intensities in the plot were measured from the height of the zero gradient EPR signal obtained at the beginning of every 3D data acquisition.

We successfully obtained 3D images of a short-lifetime nitroxyl spin probe such as TEMPOL-d_{17}, $-^{15}N$. Fig. 7 shows the surface-rendered images of TEMPOL-d_{17}, $-^{15}N$ and hydroxymethyl-PROXYL in mouse heads. The isosurface level that was used for surface rendering of 3D images was set at half of the maximum intensity. The FOV of both images was 50 mm for 128 pixels. Slice images of TEMPOL-d_{17}, $-^{15}N$ (Fig. 7C) and hydroxymethyl-PROXYL (Fig. 7D)

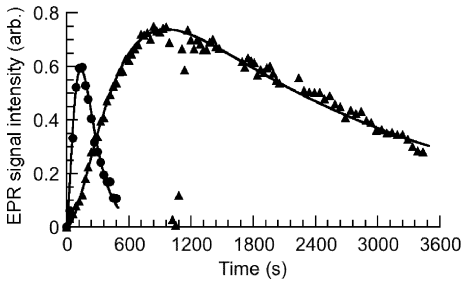

Fig. 6. EPR signal intensities of TEMPOL-d_{17}, $-^{15}N$ (closed circles) and hydroxymethyl-PROXYL (closed triangles) in the head of a mouse. Several plots for hydroxymethyl-PROXYL were perturbed at around 1000 s due to motion of the mouse being measured, which awoke from anesthesia.

were generated from the 3D image data obtained at 3 min and 15 min after infusion.

To compare the distributions of the spin probes in mouse heads, we generated slice images from the data set of 3D images. Fig. 8 shows temporal changes in axial images (*XZ*-plane) for the two kinds of spin probes. The slice thickness of these images was 3.9 mm, which corresponds to 10 pixels. The images were normalized by the maximum intensity of the resultant 2D images for each spin probe. In image processing, we used a byte scale (2^8) for the intensity of images. In axial images, free radical molecules of TEMPOL-d_{17}, $-^{15}N$ faded away quickly. We selected the position between the eyes and ears of mice for slice-selective images. The change in the spin probe distributions between the 15-min image and the 21-min image in Fig. 8C was due to displacement after the subject mouse awoke from anesthesia. Fig. 6 also shows the scattered points for EPR intensity from hydroxymethyl-PROXYL in the head of the subject mouse when the subject awoke. To validate our slice selection, we also measured a mouse (ICR mouse, weighing 30 g) with 0.5-T proton-MRI (MR-mini, MRTechnology Inc., Tsukuba, Japan). To find the position for EPR images, the *X* and *Z* positions were determined from the center of the gradient coils and the FOV of the images. For MRI images, the position was determined by the FOV and anatomical information in the images. The boundaries of the distributions of spin probes agreed well with an anatomical image obtained by proton-MRI. Since the underside of the animal was touching the lower side of the hollow cylinder (20 mm in diameter), the prominent parts of the images were shifted to the lower side. The sample space in the resonator (20 mm in diameter) was cut out from each axial image to easily compare the distributions of spin probes with the anatomical images.

4. Discussion

EPR imaging of TEMPOL-d_{17}, $-^{15}N$ in mouse head was successfully carried out under a field scanning of 0.5 s and a number of projections of 46. In in vivo EPR imaging, the acquisition time should depend on the decay of free radicals being measured. Therefore, a reduction in the acquisition time would be advantageous for in vivo EPR imaging. Potentially, 3D imaging can be performed in 13 s with field scanning of 0.15 s under the current configuration of our imager if the EPR signals are strong enough to reconstruct a 3D image. Experimental evidence suggests that our method is useful for observing the temporal and spatial changes in spin probes with a short lifetime down to a few minutes.

The use of a uniform distribution of projections is advantageous for in vivo animal imaging, since the number of projections can be reduced. The benefits of a uniform projection over conventional non-uniform projections for two-step FBP have been described in

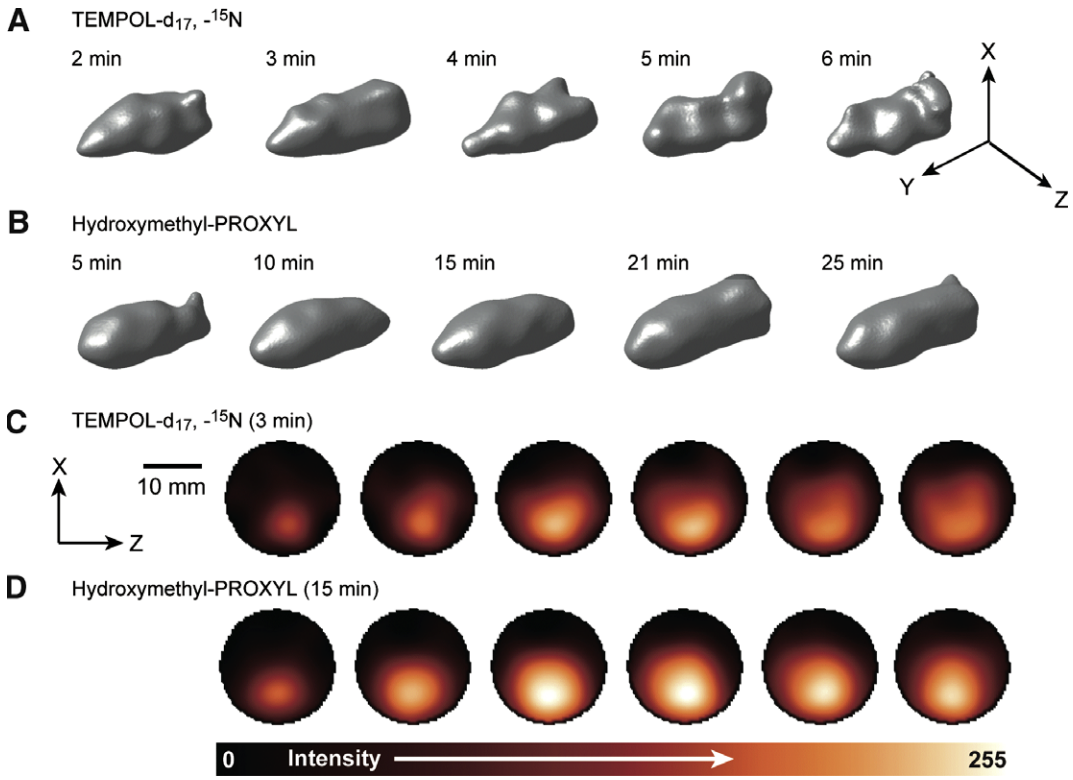

Fig. 7. 3D surface-rendered images and slice images of a mouse head. The times beside the images indicate the start time of data acquisition for each image. Time 0 indicates infusion of the spin probes. The image intensity was normalized by the maximum intensity in each 3D image. The axis of the body of the subject mouse was along the *Y*-direction. The dorsal side of the subject mouse corresponds to the upper side of the surface-rendered images. (A) Images with TEMPOL-d_{17}, $-^{15}$N probes. The measured SNRs on the zero gradient-spectrum and the spectrum with a magnetic field gradient in the *X*-direction at 3 min were 51 and 7.4, respectively. (B) Images with hydroxymethyl-PROXYL probes. The measured SNRs on the zero gradient-spectrum and a spectrum with a magnetic field gradient in the *X*-direction at 15 min were 72 and 19, respectively. The left side of the images corresponds to the nose of the subject mouse. (C) Slice images of TEMPOL-d_{17}, $-^{15}$N probes at intervals of 4 mm. Slice images cover the region from the nose (left) to the neck (right). (D) Slice images of hydroxymethyl-PROXYL probes at intervals of 4 mm.

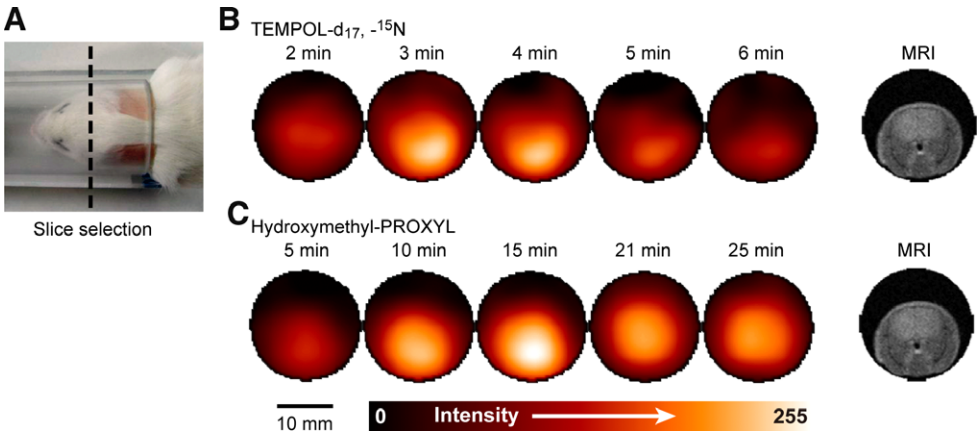

Fig. 8. Axial images of nitroxyl spin probes in a mouse head. These slice images were obtained from the data sets of 3D images. (A) Photograph of a mouse that was inserted into the tube (20 mm i.d.). (B) The distributions of TEMPOL-d_{17}, $-^{15}$N. (C) The distributions of hydroxymethyl-PROXYL. The images were trimmed by the area of the sample space in the resonator (20 mm in diameter). Proton-MRI image shows the physical arrangement of a mouse head in the resonator.

the literature [12,13]. The difference between the two methods is particularly pronounced with a small number of projections. For the non-uniform distribution method, the quality of the image showed an orientation-dependence, since non-uniform projections condensed around the polar areas of the sphere. However, for the uniform distribution method, the image quality did not depend on the orientation of the phantom. In the phantom experiment, the quality of the image obtained with 46 projections of a uniform distribution was better than that with 81 projections of a non-uniform distribution. An increase in the number of projections enhances the image quality, but also increases the total acquisition time.

The rapid data acquisition for CW-EPR imaging presented here has several features that are beneficial for the in vivo imaging of unstable spin probes, including (i) faster data acquisition for 3D CW-EPR imaging, (ii) flexible data set for post-processing, and (iii) less sensitive to non-periodic spike-like noise from the environment. A key advancement of the techniques reported here is

that a set of projection data for 3D imaging was acquired every 30 s. This makes 3D EPR imaging possible for nitroxyl spin probes that have a short-lifetime in examined animals. We can change the number of averagings for the measured spectra in post-processing of image-reconstruction, since several data sets can be recorded during the period in which nitroxyl probes are detectable. For problems regarding noise, since our data-acquisition software monitors the noise level in the baseline of EPR spectra, a spectrum that has spike-like noise can be detected and omitted. This can also reduce the time required for data acquisition; otherwise we would need to start again to obtain all of the projections. On the other hand, there are several factors that limit the further reduction of the acquisition time in CW-EPR imaging: (i) sensitivity of the spectrometer, (ii) rise/fall times of a bipolar power supply, and (iii) passage-effect of EPR spectra. When we use fast field scanning, the time constant of the lock-in amplifier should be decreased. This leads to a decrease in the SNR for a single-scan spectrum. If multiple-scan EPR spectra are allowed in a given application, this issue of the SNR will not be problematic. However, a shorter acquisition time results in a degraded SNR even if 3D EPR imaging can be performed in a limited time. The shortest rise/fall time of a ramp-signal from 0 to 10 A was 50 ms for the bipolar power supply we used.

CW-EPR imaging is a practical solution to the visualization of free radical molecules that have a short relaxation time in animal subjects, and several methods are available to reduce the acquisition time of EPR imaging for small rodents: (i) pulsed EPR method [21–24], (ii) rapid-scan EPR method [25–28], (iii) EPR imaging using spinning magnetic field gradients [29,30], and (iv) uniform distribution of projections [12–15]. While pulsed EPR imaging has been intensively developed for animal imaging over the past decade, it is limited to free radical species that have a longer relaxation time, on the order of microseconds. In contrast, rapid-scan EPR spectroscopy can be applied to free radicals that have a shorter relaxation time of unpaired electrons. This method can achieve a repetition rate of 30 kHz for data acquisition [26]. However, in vivo imaging based on rapid-scan EPR spectroscopy has not yet been reported on small rodents. In addition, field inhomogeneities caused by eddy currents result in the broadening of EPR spectra [26]. EPR imaging using spinning magnetic field gradients has been reported for images of lithium phthalocyanine crystals and solutions of free radicals [29,30]. Spinning gradient EPR imaging has not yet been performed with living animals. A uniform distribution of projections is a straightforward manner to reduce the projection number. This approach regarding the setting of projections can be combined with the instrumental methods described above.

A lower SNR forces the use of a lower cut-off frequency for the Hamming filter in image-reconstruction. Otherwise, considerable noise appears in the reconstructed images, which causes blurring. Since the intrinsic line-width $\Delta B_{1/2}$ of TEMPOL-d_{17}, $-^{15}N$ was 0.15 mT and the field gradient G was 40 mT/m, the spatial resolution can be estimated to be $\Delta B_{1/2}/G = 3.8$ mm. The line-width $\Delta B_{1/2}$ was estimated from the zero gradient-spectra obtained from the mouse head. Although broadening of the line-width occurred for injected TEMPOL-d_{17}, $-^{15}N$ (200 mM), the concentration of TEMPOL-d_{17}, $-^{15}N$ was not so high in tissues in the head. Thus, the zero gradient EPR spectra retained a narrower line-width. If a process of deconvolution to further enhance the resolution works well, the resolution can be approximately doubled [31]. Nevertheless, the images in Figs. 7C, 8B and C were very blurred. This is because the low-pass window function sacrificed the high-frequency components of the spatial distribution of the spin probes. In this case, spatial resolution could be improved by superresolution EPR imaging techniques, i.e., iterative deconvolution techniques [32,33]. However, the detailed discussion of methods to deblur images are beyond the scope of this article.

When nitroxyls are injected into small animals, most readily disappear, depending on their reduction reaction and excretion rates. The very short transverse relaxation times (T_2) of commonly used probes such as nitroxyls in vivo do not easily allow them to be studied using pulsed EPR spectroscopy, and thus they are conveniently detected and imaged by CW-EPR. Therefore, the biggest challenge in EPR imaging is the very rapid acquisition of EPR spectra from living specimens by CW-EPR. To attack the problem shown above, a reasonably fast EPR imaging system using fewer projections was introduced in the present study. These instrumental achievements allow us to use many different kinds of spin probes for various biomedical applications, regardless of their lifetime in living organisms or their chemical structures.

5. Conclusions

The temporal change in infused TEMPOL-d_{17}, $-^{15}N$ in mouse heads was successfully visualized with 3D CW-EPR imaging. Fast data acquisition was achieved at 0.65 s/projection, which was twice as fast as that with state-of-the-art CW-EPR imaging as reported by Samouilov et al. Our results suggest that 3D CW-EPR imaging can be used with nitroxyl spin probes that have a half-life of a few minutes in live animals. This should be useful for studies on pharmacokinetics, drug delivery, and in vivo free-radical-related molecular imaging.

Acknowledgments

The authors are grateful to Dr. Murali C. Krishna, National Cancer Institute, National Institutes of Health, Bethesda, MD, for a critical reading of the manuscript, and Hitoshi Susaki, Yamagata University, for his assistance with hardware development. This work was supported by a grant from the Japan Society for the Promotion of Science (18360195 to H.H.).

References

[1] L.J. Berliner, H. Fujii, X.M. Wan, S.J. Lukiewicz, Feasibility study of imaging a living murine tumor by electron paramagnetic resonance, Magn. Reson. Med. 4 (1987) 380–384.
[2] P. Kuppusamy, J.L. Zweier, Cardiac applications of EPR imaging, NMR Biomed. 17 (2004) 226–239.
[3] H. Yokoyama, Y. Lin, O. Itoh, Y. Ueda, A. Nakajima, T. Ogata, T. Sato, H. Ohya-Nishiguchi, H. Kamada, EPR imaging for in vivo analysis of the half-life of a nitroxide radical in the hippocampus and cerebral cortex of rats after epileptic seizures, Free Radic. Biol. Med. 27 (1999) 442–448.
[4] J.P. Kao, E.D. Barth, S.R. Burks, P. Smithback, C. Mailer, K.H. Ahn, H.J. Halpern, G.M. Rosen, Very-low-frequency electron paramagnetic resonance (EPR) imaging of nitroxide-loaded cells, Magn. Reson. Med. 58 (2007) 850–854.
[5] J. Shen, S. Liu, M. Miyake, W. Liu, A. Pritchard, J.P. Kao, G.M. Rosen, Y. Tong, K.J. Liu, Use of 3-acetoxymethoxycarbonyl-2,2,5,5-tetramethyl-1-pyrrolidinyloxyl as an EPR oximetry probe: potential for in vivo measurement of tissue oxygenation in mouse brain, Magn. Reson. Med. 55 (2006) 1433–1440.
[6] F. Demsar, T. Walczak, P.D. Morse II, G. Bacic, Z. Zolnai, H.M. Swartz, Detection of diffusion and distribution of oxygen by fast-scan EPR imaging, J. Magn. Reson. 76 (1988) 224–231.
[7] S. Ishida, H. Kumashiro, N. Tsuchihashi, T. Ogata, M. Ono, H. Kamada, E. Yoshida, In vivo analysis of nitroxide radicals injected into small animals by L-band ESR technique, Phys. Med. Biol. 34 (1989) 1317–1323.
[8] M. Alecci, S. Colacicchi, P.L. Indovina, F. Momo, P. Pavone, A. Sotgiu, Three-dimensional in vivo ESR imaging in rats, Magn. Reson. Imaging 8 (1990) 59–63.
[9] S. Ishida, S. Matsumoto, H. Yokoyama, N. Mori, H. Kumashiro, N. Tsuchihashi, T. Ogata, M. Yamada, M. Ono, T. Kitajima, H. Kamada, E. Yoshida, An ESR-CT imaging of the head of a living rat receiving an administration of a nitroxide radical, Magn. Reson. Imaging 10 (1992) 109–114.
[10] H. Yokoyama, T. Ogata, N. Tsuchihashi, M. Hiramatsu, N. Mori, A spatiotemporal study on the distribution of intraperitoneally injected nitroxide radical in the rat head using an in vivo ESR imaging system, Magn. Reson. Imaging 14 (1996) 559–563.
[11] A. Samouilov, G.L. Caia, E. Kesselring, S. Petryakov, T. Wasowicz, J.L. Zweier, Development of a hybrid EPR/NMR coimaging system, Magn. Reson. Med. 58 (2007) 156–166.
[12] Y. Deng, P. Kuppusamy, J.L. Zweier, Progressive EPR imaging with adaptive projection acquisition, J. Magn. Reson. 174 (2005) 177–187.

[13] R. Ahmad, Y. Deng, D.S. Vikram, B. Clymer, P. Srinivasan, J.L. Zweier, P. Kuppusamy, Quasi Monte Carlo-based isotropic distribution of gradient directions for improved reconstruction quality of 3D EPR imaging, J. Magn. Reson. 184 (2007) 236–245.
[14] K.H. Ahn, H.J. Halpern, Spatially uniform sampling in 4-D EPR spectral-spatial imaging, J. Magn. Reson. 185 (2007) 152–158.
[15] R. Ahmad, D.S. Vikram, B. Clymer, L.C. Potter, Y. Deng, P. Srinivasan, J.L. Zweier, P. Kuppusamy, Uniform distribution of projection data for improved reconstruction quality of 4D EPR imaging, J. Magn. Reson. 187 (2007) 277–287.
[16] P. Kuppusamy, P. Wang, J.L. Zweier, M.C. Krishna, J.B. Mitchell, L. Ma, C.E. Trimble, C.J.C. Hsia, Electron paramagnetic resonance imaging of rat heart with nitroxide and polynitroxyl-albumin, Biochemistry 35 (1996) 7051–7057.
[17] Y. Kawada, H. Hirata, H. Fujii, Use of multi-coil parallel-gap resonators for co-registration EPR/NMR imaging, J. Magn. Reson. 184 (2007) 29–38.
[18] H. Hirata, G. He, Y. Deng, I. Salikhov, S. Petryakov, J.L. Zweier, A loop resonator for slice-selective in vivo EPR imaging in rats, J. Magn. Reson. 190 (2008) 124–134.
[19] L.C. Maier Jr, J.C. Slater, Field strength measurements in resonant cavities, J. Appl. Phys. 23 (1952) 68–77.
[20] J.H. Freed, D.S. Leniart, J.S. Hyde, Theory of saturation and double resonance effects in ESR spectra: Ill rf coherence and line shapes, J. Chem. Phys. 47 (1967) 2762–2773.
[21] J. Bourg, M.C. K rishna, J.B. Mitchell, R.G. Tschundin, T.J. Pohida, W.S. Friauf, P.D. Smith, J. Metcalfe, F. Harrington, S. Subramanian, Radiofrequency FT EPR spectroscopy and imaging, J. Magn. Reson. Ser. B 102 (1993) 112–115.
[22] S. Subramanian, N. Devasahayam, R. Murgesan, K. Yamada, J. Cook, A. Taube, J.B. Mitchell, J.A.B. Lohman, M.C. Krishna, Single-point (constant-time) imaging in radiofrequency Fourier transform electron paramagnetic resonance, Magn. Reson. Med. 48 (2002) 370–379.
[23] R.H. Pursley, G. Salem, N. Devasahayam, S. Subramanian, J. Koscielniak, M.C. Krishna, T.J. Pohida, Integration of digital signal processing technologies with pulsed electron paramagnetic resonance imaging, J. Magn. Reson. 178 (2006) 220–227.
[24] C. Mailer, S.V. Sundramoorthy, C.A. Pelizzari, H.J. Halpern, Spin echo spectroscopic electron paramagnetic resonance imaging, Magn. Reson. Med. 55 (2006) 904–912.
[25] M. Tseitlin, A. Dhami, S.S. Eaton, G.R. Eaton, Comparison of maximum entropy and filtered back-projection methods to reconstruct rapid-scan EPR images, J. Magn. Reson. 184 (2007) 157–168.
[26] J.P. Joshi, G.R. Eaton, S.S. Eaton, Impact of resonator on direct-detected rapid-scan EPR at 9.8 GHz, Appl. Magn. Reson. 28 (2005) 239–249.
[27] J.W. Stoner, D. Szymanski, S.S. Eaton, R.W. Quine, G.A. Rinard, G.R. Eaton, Direct-detected rapid-scan EPR at 250 MHz, J. Magn. Reson. 170 (2004) 127–135.
[28] J.P. Joshi, J.R. Ballard, G.A. Rinard, R.W. Quine, S.S. Eaton, G.R. Eaton, Rapid-scan EPR with triangular scans and Fourier deconvolution to recover the slow-scan spectrum, J. Magn. Reson. 175 (2005) 44–51.
[29] K. Ohno, M. Watanabe, Electron paramagnetic resonance imaging using magnetic-field-gradient spinning, J. Magn. Reson. 143 (2000) 274–279.
[30] Y. Deng, G. He, S. Petryakov, P. Kuppusamy, J.L. Zweier, Fast EPR imaging at 300 MHz using spinning magnetic field gradient, J. Magn. Reson. 168 (2004) 220–227.
[31] F. Momo, S. Colacicchi, A. Sotgiu, Limits of deconvolution in enhancing the resolution in EPR imaging experiments, Meas. Sci. Technol. 4 (1993) 60–64.
[32] H. Hirata, M. Wakana, H. Susaki, Feasibility study of superresolution continuous-wave electron paramagnetic resonance imaging, Appl. Phys. Lett. 88 (2006) 254103.
[33] R. Ahmad, B. Clymer, D.S. Vikram, Y. Deng, H. Hirata, J.L. Zweier, P. Kuppusamy, Enhanced resolution for EPR imaging by two-step deblurring, J. Magn. Reson. 184 (2007) 246–257.